Endothelial Cilia Mediate Low Flow Sensing during Zebrafish Vascular Development

Jacky G. Goetz, Emily Steed, Rita R. Ferreira, Stéphane Roth, Caroline Ramspacher, Francesco Boselli, Gilles Charvin, Michael Liebling, Claire Wyart, Yannick Schwab, et al.

Cell Reports
Report

Endothelial Cilia Mediate Low Flow Sensing during Zebrafish Vascular Development

Jacky G. Goetz,[1,2,3,4,11] Emily Steed,[1,2,3,4] Rita R. Ferreira,[1,2,3,4] Stéphane Roth,[1,2,3,4] Caroline Ramspacher,[1,2,3,4] Francesco Boselli,[1,2,3,4] Gilles Charvin,[1,2,3,4] Michael Liebling,[5] Claire Wyart,[6,7,8,9] Yannick Schwab,[10] and Julien Vermot[1,2,3,4,*]

[1]Institut de Génétique et de Biologie Moléculaire et Cellulaire, 67400 Illkirch, France
[2]Centre National de la Recherche Scientifique, UMR7104, 67404 Illkirch, France
[3]Institut National de la Santé et de la Recherche Médicale, U964, 67404 Illkirch, France
[4]Université de Strasbourg, 67404 Illkirch, France
[5]Department of Electrical and Computer Engineering, University of California, Santa Barbara, Santa Barbara, CA 93106, USA
[6]Institut du Cerveau et de la Moelle Épinière (ICM), Hôpital de la Pitié-Salpêtrière, 75013 Paris, France
[7]Inserm UMRS 1127, 75013 Paris, France
[8]CNRS UMR 7225, 75013 Paris, France
[9]UPMC University of Paris 06, 75005 Paris, France
[10]Electron Microscopy Core Facility, Cell Biology and Biophysics Unit, European Molecular Biology Laboratory, Meyerhofstrasse 1, 69117 Heidelberg, Germany
[11]Present address: Inserm U1109, The Microenvironmental Niche in Tumorigenesis and Targeted Therapy, 67200 Strasbourg, France; LabEx Medalis, Fédération de Médecine Translationnelle de Strasbourg (FMTS), 67000 Strasbourg, France
*Correspondence: julien@igbmc.fr
http://dx.doi.org/10.1016/j.celrep.2014.01.032

SUMMARY

The pattern of blood flow has long been thought to play a significant role in vascular morphogenesis, yet the flow-sensing mechanism that is involved at early embryonic stages, when flow forces are low, remains unclear. It has been proposed that endothelial cells use primary cilia to sense flow, but this has never been tested in vivo. Here we show, by non-invasive, high-resolution imaging of live zebrafish embryos, that endothelial cilia progressively deflect at the onset of blood flow and that the deflection angle correlates with calcium levels in endothelial cells. We demonstrate that alterations in shear stress, ciliogenesis, or expression of the calcium channel PKD2 impair the endothelial calcium level and both increase and perturb vascular morphogenesis. Altogether, these results demonstrate that endothelial cilia constitute a highly sensitive structure that permits the detection of low shear forces during vascular morphogenesis.

INTRODUCTION

The formation of a functional cardiovascular system relies on a complex interplay among a genetic program, fluid mechanics, and processes of cellular reorganization (Potente et al., 2011; Herbert and Stainier, 2011). Although the genetics of flow-inducible genes have been extensively analyzed over the last few years (Buschmann et al., 2010; Bussmann et al., 2011; Chen et al., 2012; Corti et al., 2011; le Noble et al., 2004; Nicoli et al., 2010), much less is known about the blood-flow-sensing mechanisms used during vascular development. Numerous in vitro studies have demonstrated that vascular endothelial cells (ECs) can both sense and transduce biomechanical stimuli, such as wall shear stress, through primary cilia (Hierck et al., 2008; Nauli et al., 2008). However, a quantitative understanding of the flow conditions sensed by cilia and an assessment of their function within the intact developing vascular network are still lacking. Moreover, the potential involvement of cilia in sensing flow forces of small amplitude, such as those observed in early embryonic stages, remains unclear.

RESULTS

Because we expected flow forces to vary greatly at the onset of flow, we first characterized the flow conditions generated over time during the early embryonic stages when flow begins (Forouhar et al., 2006). The flow features in the vascular network directly depend on heart function. We thus followed heart morphology (Figure 1A; Movie S1) and contraction between 24 and 28 hr postfertilization (hpf). At 24 hpf, we could not detect the opening of the endocardial lumen. To quantitate this, we measured the linear deformation of both the endocardium and myocardium, and found they remained low (90%) and very low (18%), respectively (Figures 1A–1C and S1A–S1C; Movies S1, S2, and S5). This means that even though the myocardium contracts significantly, the endocardium does not open properly and strongly limits flow forces. By comparison, the inner structure of the endocardial lumen displayed a clear opening of the

Cell PRESS
Open ACCESS

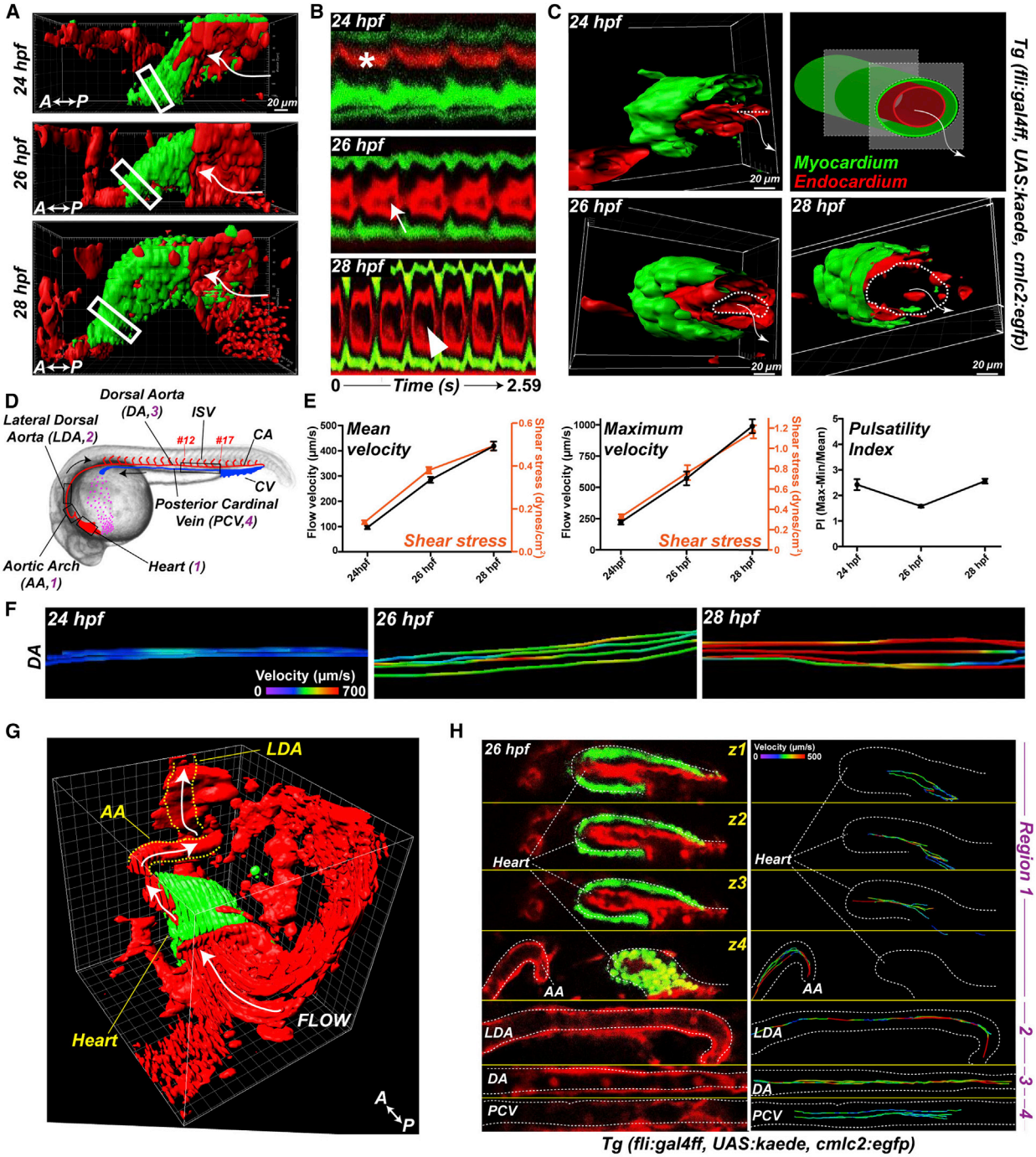

(legend on next page)

endocardium (dashed lines) at 26 hpf (Figures 1A–1C, S1B, and S1C; Movies S3 and S5). Consistently, the linear deformation of the endocardium reached 197% at 26 hpf, whereas the myocardium displayed only a mild increase to 40% (Figure S1C; Movies S3 and S5). At 28 hpf, the heartbeat significantly increased (2.63 ± 0.17 Hz), as did the endocardial linear deformation to 283% (75% for the myocardium; Figures 1A–1C and S1A–S1C; Movies S1, S4, and S5). Altogether, these data show that endocardial deformation is the major factor controlling heart pumping efficiency at these early stages.

Because the vascular network is complex and flow forces directly depend on the anatomy of the network, we next characterized the flow along the network. Between 24 and 28 hpf, we found that flow increased almost linearly in the dorsal aorta (DA), whereas pulsatility remained steady (Figures 1E and 1F; Movie S6). We also analyzed the flow velocities at the heart exit and further downstream in the network at 26 hpf. Blood cells exit the heart into the ventral aorta, which branches into the mandibular aortic arches (AAs) (Isogai et al., 2001; Figures 1D, 1G, S1D, and S1E; Movie S7). The arches empty directly into the two (left and right) lateral dorsal aortas (LDAs), draining blood into the medial DA (Isogai et al., 2001; Figures 1D, 1G, S1D, and S1E; Movie S7). Blood-flow velocity peaks in the AA and LDA reached 883 ± 118 and 1159 ± 187 μm/s, respectively, although the mean velocities were 192 ± 13 and 170 ± 15 μm/s, respectively (Figures 1G–1I and S1E; Movie S7). Altogether, these data demonstrate that flow profiles vary extensively along the vascular network and with the developmental stage due to heart remodeling. It also suggests that every area of the network is in contact with unique flow profiles during the onset of flow.

Detecting such variability in intravascular flow necessitates a very sensitive mechanism of flow sensing. Flow velocity is considerably slower along the vessel wall than at its center, because viscous friction prevents fluid from slipping on the vessel wall (Freund et al., 2012; Supatto and Vermot, 2011). In this context, cilia protrusion allows flow to be sensed away from the cell membrane, and therefore constitutes an advantageous structure for low-amplitude flow sensing. To determine the distribution of endothelial cilia in vivo, we analyzed a double-transgenic line, *Tg(β-actin:arl13b-egfp; flk1:mCherry)*, labeling cilia and ECs, respectively. We found that most ECs displayed cilia protruding into the aorta and vein lumen between 24 and 28 hpf (at 28 hpf, 76% [934/1,271 cells] of the ECs in the caudal artery [CA] and vein [CV] are ciliated; Figures 2A–2D; see also Movie S8, left panel). Cilia were reduced in number at later stages and almost absent in the CA and CV at 48 hpf (4%, 31/996 cells), suggesting that cilia are necessary when flow forces are low, during the time of vascular morphogenesis. To confirm this hypothesis, we analyzed cilia distribution in *tnnt2a* morphants, which lack a functional *troponin T2a* gene, a key component of the heart muscle thin filaments specific to the myocardium (Sehnert et al., 2002), thus resulting in noncontractile hearts. We found that 68% of ECs (742/1,091) remained ciliated in the absence of flow. These observations are consistent with earlier in vitro studies suggesting that high shear stress can disassemble cilia (Iomini et al., 2004).

Using correlative microscopy approaches, we next characterized the 3D ultrastructure of endothelial cilia by electron microscopy (EM) coupled to electron tomography in order to precisely assess the endothelial cilia deformation in conjunction with its ultrastructure. Using a set of anatomical landmarks, we focused on different cilia, located in the CA (arterial; Figures 2A–2D, 2F–2M, and S2B–S2D; Movies S8, S9, S10, and S11) and the CV (venous; Figures 2E and S2A). We then generated thick (~250 nm) serial sections of the region of interest and reassembled 16 consecutive tomograms to reconstruct 4 μm of the protruding cilia near the cell surface (Figures 2F–2L and S2B–S2D; Movies S9 and S10). We found that the basal body displayed a canonical 9-fold symmetry and was composed of nine microtubule triplets regularly spaced and linked to transition fibers in the region most proximal to the plasma membrane (Figures 2F and 2I–2L; Movies S9 and S10). Remarkably, we observed the rapid disappearance of some microtubules (red, Figure 2M; Movie S11) in the most distal extracellular region of the axoneme. Given that microtubules are known to confer stiffness to the structures they shape (Hoey et al., 2012), we reasoned that this unusual arrangement could give endothelial cilia unique stiffness profiles. To test this hypothesis, we modeled the cilium as a beam and computed the hydrodynamic load by the local slender-body theory. The bending stiffness is defined as $E_b = M/k$, with k being the curvature and M the moment at a cross-section of the cilium. Using our in vivo measurements, we estimated the bending stiffness (E_b) of endothelial cilia to be in the range of $0.5 < E_b < 1 \times 10^{-23}$ Nm^2, making them softer than kidney cilia previously examined in vitro ($1 < E_b < 5 \times 10^{-23}$ Nm^2) (Young et al., 2012), possibly due to their

Figure 1. Early Cardiac Morphometrics and Subsequent Hemodynamics at Blood Flow Onset

(A) 3D imaging of the heartbeat in *Tg(fli:gal4FF; UAS:kaede; cmlc2:egfp)* embryos. Heart myocardium is labeled in green (GFP), and endocardium and blood cells are in red (photoconverted Kaede).

(B) Kymographs of a section (boxed region) of the heart tube. The asterisk indicates the absence of a visible endocardial lumen at 24 hpf. The arrows indicate the progressive opening of the lumen at 26 and 30 hpf.

(C) 3D sections of the boxed regions in (A). The dashed lines underline the endocardium opening and the arrows show the flow direction.

(D) Simplified view of the cardiovascular system of 24–28 hpf embryos. CA, caudal artery; CV, caudal vein; ISV, intersomitic vessels.

(E) Blood cell tracking in the developing DA (see box in D). Graphs show the mean and maximum flow velocity in the DA (see box in D) and the pulsatility index (PI) at 24, 26, and 28 hpf.

(F) Tracks in the DA are color-coded for their instantaneous velocity over time.

(G) 3D anatomy of a 26 hpf heart and its neighboring vasculature and flow direction. See also Movies S5 and S7.

(H) Vascular hemodynamics in a single embryo. Three sections of the same heart are displayed (see corresponding regions in D). Tracks are color-coded for their instantaneous velocity over time.

(I) Plots of the velocity and PI observed in a single embryo.

Error bars depict SEM. Statistical significance was determined by unpaired Student's t test; *$p < 0.05$, **$p < 0.01$, ***$p < 0.001$. See also Figure S1.

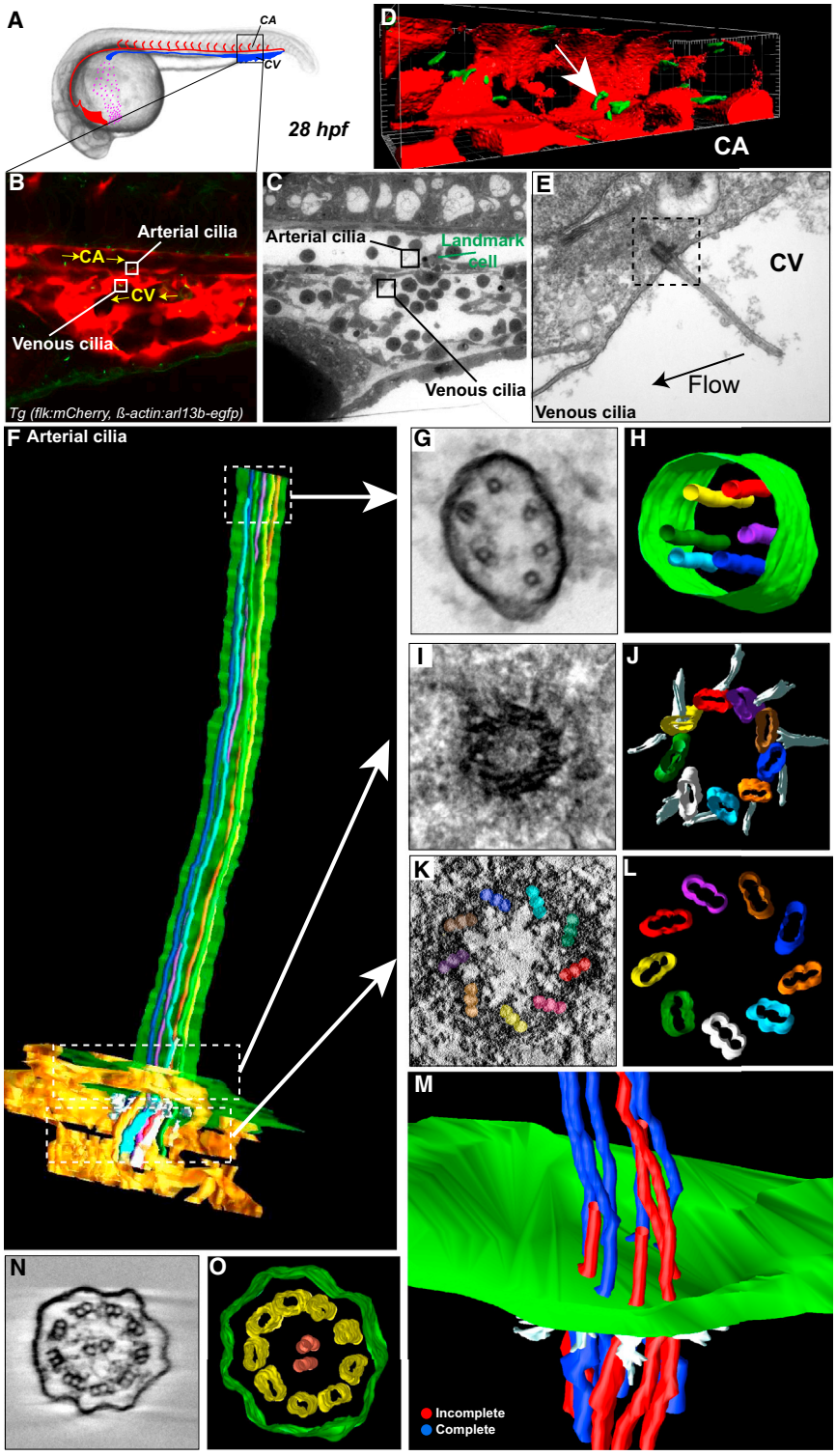

Figure 2. Early Embryonic Vessels Are Ciliated

(A) Global view of a 28 hpf embryo.

(B) Single confocal section of the region of interest in the CA; endothelium is in red, primary cilia are in green. Boxes define two cilia of interest located in the CA (arterial) and CV (venous). Flow direction is indicated. See also Movie S8.

(C) Transmission electron microscopy (TEM) image of the region shown in (B).

(D) 3D reconstruction of the region of interest (arrow points to cilium of interest).

(E) TEM image of the venous cilia highlighted in (B) and (C).

(F–M) Electron tomography of the arterial cilia outlined in (B)–(D).

(F) Reconstruction of the portion of the protruding cilia near the cell surface.

(G–L) Single tomograms and modeling of regions located in the axoneme (G and H) and the basal body (I–L) are presented. Microtubules were color-labeled along the whole cilia. Note that the light blue microtubule is incomplete over the tomogram presented in (G) and (H). See also Movies S8, S9, and S10.

(M) A portion of the cilia proximal to the plasma membrane. Microtubules that disappear along the cilia axis are labeled in red. See also Movie S11.

(N and O) Single tomogram and modeling of a motile cilia located in the pronephros. Note the characteristic 9+2 microtubule doublet architecture.

See also Figure S2 and Movie S12.

unique microtubule content. This low-microtubule feature was seen in all of the observed cilia regardless of vessel identity and position in the network (Figure S2). As expected, pronephric motile cilia of the same animal displayed the conventional 9+2 microtubule doublets in the axoneme (Figures 2N and 2O; Movie S12), demonstrating that the sample preparation did not affect the native cilia ultrastructure. We also tested whether blood flow is involved in controlling the endothelial cilia microtubule content by characterizing the endothelial cilia ultrastructure in controls at 24 hpf, when flow forces are extremely low, and in the silent heart mutants (*sih*), which lack a functional *tnnt2a* gene (Sehnert et al., 2002; Figure S2E). In the absence of flow, the observed cilia ultrastructure was similar to that of controls, suggesting that flow does not affect the microtubule content of endothelial cilia. Together, these results suggest that endothelial cilia have a unique ultrastructure, which by dictating rigidity and bending properties may render the cilia deformable in response to small flow variations.

To examine this, we tested the sensitivity of cilia deflection at the earliest stages of flow generation and characterized the relationship between blood flow and cilia bending. We segmented cilia based on their GFP signal and plotted the most acute value

of the angle between the cilia and the endothelial surface over time (Figures 3A–3C; Movie S13), while simultaneously imaging flow (Figure 3C; Movie S13). At 24 hpf, we found the average cilia angle in the DA lumen to be close to 84° (Figures 3D, 3F, and S3; Movie S14). This angle progressively decreased with time, reaching 41.5° ± 2° at 28 hpf (Figures 3D, 3F, and S3A; Movie S14), when cilia are highly deflected by flow. We also found that the frequency of cilia bending resembled that of the blood flow in response to heart contraction (2.41 Hz and 2.63 ± 0.17 Hz, respectively (Figures S1A, S3A, and S3B). Without flow in the *tnnt2a* morphants, endothelial cilia were not deflected (average angle 96° ± 2.2°; Figures 3H and 3I; Movie S15). Furthermore, although the absence of blood cells in *gata1* morphants did not affect the mean flow velocity (Figure 3J; Movie S16) or frequency of cilia deflection (Figure S3H), the cilia angle was less acute (58° versus 42° for controls), showing that cilia deflection also depends on blood viscosity (Figures 3H, 3I, and S3H; Movie S17). We conclude that cilia can be deflected by subtle changes in hemodynamic forces in the vascular network.

Because cilia deflection has been proposed to increase calcium signaling in vitro in kidney epithelial (Nauli et al., 2003) and EC cultures (Nauli et al., 2008), we next investigated whether endothelial cilia bending correlated with increased calcium signaling in vivo. Using the endothelial-specific expression of a genetically encoded calcium indicator, *Tg(fli:gal4ff; UAS:gcamp3.0)* (Warp et al., 2012), we observed a progressive increase in calcium levels in the DA during blood flow onset from 24 to 28 hpf (Figures 3E and 3G), consistent with the progressive flow-mediated cilia deflection between these stages (Figures 3D and 3F). At 28 hpf, we also observed a gradation in both cilia deflection and calcium content along the DA anteroposterior axis (Figures S3C–S3G), as well as a clear difference in both parameters between arterial cilia (located in the DA) and venous cilia (located in the PCV) (Figures S3C–S3G). These results indicate that changes in vascular flow velocities correlate with a specific cilia deflection angle and calcium level at every point in the vascular network. We also found that the absence of flow in *sih* mutants, as well as a strong reduction in heart contractility in *cmlc1* morphants (Meder et al., 2009), led to a dramatic decrease in EC calcium levels (Figures 3K and S4A–S4D), showing that cilia and flow are necessary to control intracellular calcium entry in ECs. We observed similar defects when blood viscosity was reduced in *gata1* morphants. The absence of *gata1* stopped red blood cell production, and plasma flow had the same average speed as observed in controls (Figure 3J). This allowed us to test the impact of decreased viscosity on cilia bending (Figures 3H and 3I). We observed similar defects in these conditions (Figure 3K). Cilia deflection is thus extremely sensitive to low-shear forces and enables subtle changes in hemodynamic forces to be transduced into differential calcium levels inside the EC.

Cilia mechanodetection and calcium signaling depend on the calcium-permeable channel PKD2/PC2/TRPP2 in several ciliated structures, such as the left-right organizer (McGrath et al., 2003; Yoshiba et al., 2012), kidney epithelial cells (Nauli et al., 2003), and cultured ECs (mouse and human) (AbouAlaiwi et al., 2009). We found that *pkd2* was expressed in the developing vascular network and that PKD2 was located in membranous structures close to the base of the cilia (Figure S4E). As in *sih* embryos, depletion of *pkd2* reduced endothelial calcium levels (Figures 3K, S4A, and S4D). These phenotypes were also observed upon spatiotemporal knockdown of *pkd2* using a photo-morpholino (photo-MO) to specifically initiate knockdown of *pkd2* in the caudal plexus at 22 hpf (Figures 3K and S4H–S4L). We additionally tested the role of cilia in the process by knocking down *ift88* (Kramer-Zucker et al., 2005; Tsujikawa and Malicki, 2004), a protein that is critical for ciliogenesis, using regular and photo-MOs (Figures S4M–S4U). Similar reductions in calcium levels were observed in the absence of endothelial cilia in both *ift88* morphants and *ift88* photomorphants when activated at 21 hpf (Figures S4N–S4U), further suggesting that flow acts through endothelial cilia to control calcium increase (Figure 3I). In all cases, loss of *pkd2* and endothelial cilia led to impaired calcium influx (Figures 3K, S4A–S4D, S4L, and S4T) but had no effect on the average blood flow velocity (Figures 3J, S4K, S4Q, and S4U) or cilia deflection in the case of *pkd2* morphants (Figure 3H). These results suggest that endothelial cilia-mediated mechanodetection depends on PKD2.

Flow function is highly diverse during angiogenesis and can induce vessel remodeling (Nicoli et al., 2010) or stabilization according to the vessel type (Potente et al., 2011). To test the possible influence of flow and endothelial cilia on the development of embryonic blood vessels, we studied the effects of the absence of blood flow at the primitive heart stage by knocking down *tnnt2a*. We then analyzed the formation of the caudal plexus, which is highly remodeled to form a functional CV during the time period in which endothelial cilia are visible. We observed that the absence of flow dramatically impaired remodeling of the CV. This morphological defect was associated with a decreased protrusive activity and reduced numbers of venous sprouts, vascular loops, and total ECs (Figures 4A–4C; Movies S18 and S19). Furthermore, we found that the absence of flow also led to a significant reduction in overall EC numbers in both the CA and CV (Figures 4C and S4C). Absence of flow did not affect intersomitic vessel (ISV) formation, confirming the fact that flow is not absolutely required for tip cell specification and migration (Isogai et al., 2003). Importantly, low blood viscosity in the *gata1* morphants led to intermediate phenotypes in terms of protrusive activity (Figure 4A), number of vascular loops (Figure 4B; Movie S19), and EC numbers in the CV (Figure 4C). This correlates with the intermediate values observed for calcium levels in these morphants (Figures 3K and S4A) and further suggests that there is a tight correlation between cilia deflection levels and the extent of vascular remodeling. Furthermore, these results confirm that the observed phenotypes are not due to perturbations in the circulating plasma factors involved in vascular development; plasma flow can still carry important diffusible molecules such as S1P1 and BMP10 (Gaengel et al., 2012; Jung et al., 2012; Laux et al., 2013; Ben Shoham et al., 2012). Similarly, loss of *pkd2* and *ift88* through regular and conditional knockdown all led to impaired morphogenesis of the CV (Figures 4A–4C, S4F, S4G, S4I, S4N, and S4S). Indeed, the defects were associated with a decreased number and activity of venous sprouts (Figure 4A), vascular loops (Figures 4B, S4F, S4I, S4N, S4O, S4S, S4T; Movie S19), and EC numbers (Figure 4C), but without altering the blood flow (Figures 3J, S4K, S4Q, and S4U) or ISV development.

Cell PRESS
Open ACCESS

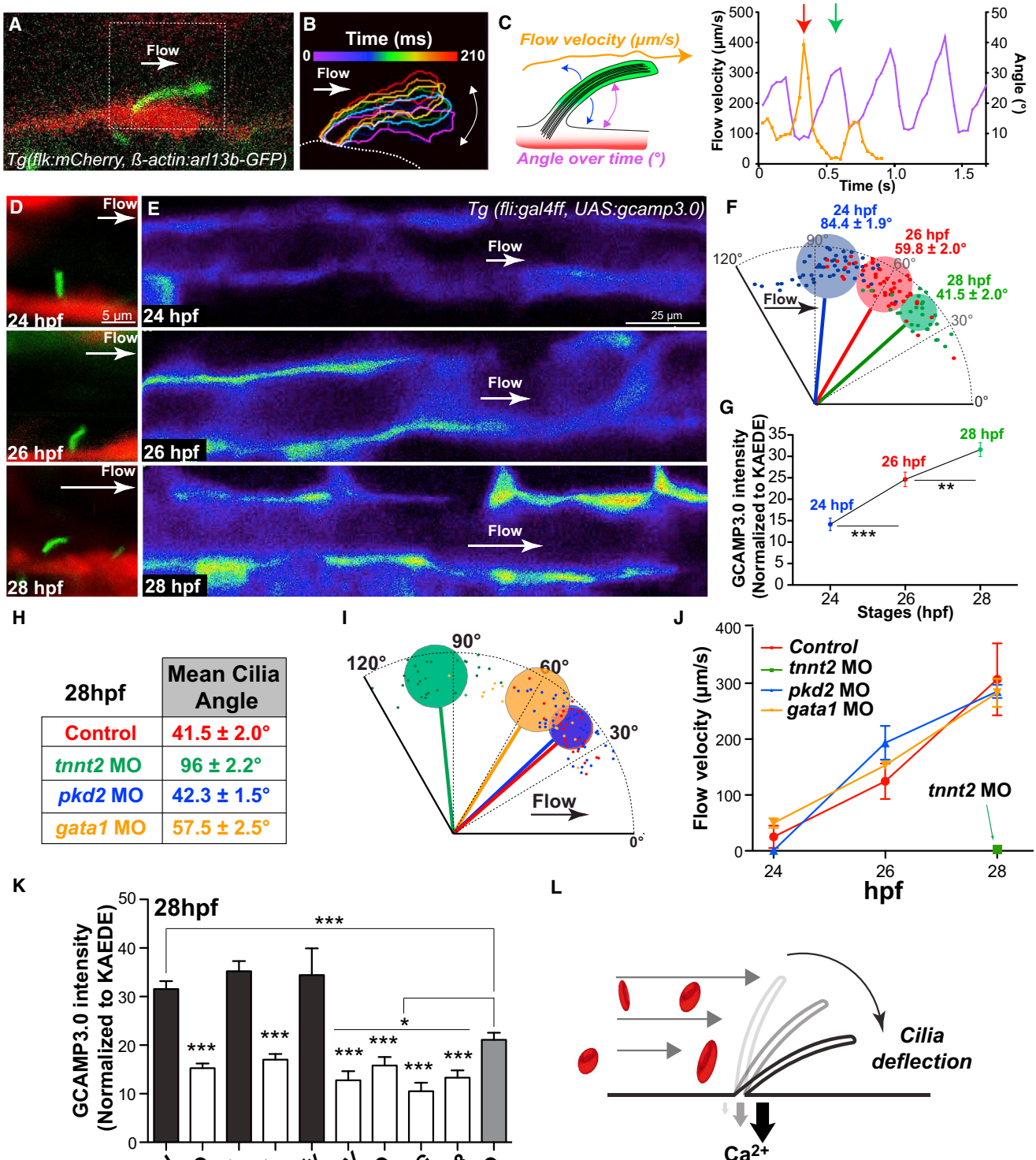

(legend on next page)

DISCUSSION

Through the use of primary cilia, ECs can sense extraordinarily low flow forces and discriminate between the very subtle variations in flow regimes generated along the developing vascular network. The relative simplicity of the zebrafish vascular network provides an ideal system in which to elucidate mechanotransduction mechanisms that could also be of significance in more complex organisms, such as humans. Although published work in mammalian systems has not identified a specific requirement for PKD2 signaling in venous angiogenesis (Garcia-Gonzalez et al., 2010), mammalian vascular systems are more complex, and the requirement for cilia during early development makes specific interrogation of later time points difficult (Oh and Katsanis, 2012). Given that we demonstrate the involvement of cilia in the sensing of low flow forces, it would be particularly interesting to study developmental programs that rely on such flow profiles, such as early cardiogenesis, lymphatic-valve formation, hematopoiesis, and tumor angiogenesis. In addition, vascular defects, such as atherosclerosis (Rydholm et al., 2010), have been linked to cilia and the detection of disturbed flow in humans, implying a pathological relevance to cilia-mediated flow sensing. Furthermore, specific loss of function of PKD2 in ECs has been implicated in angiogenesis defects in the placenta, which is an area of low flow forces (Garcia-Gonzalez et al., 2010). Thus, determining the precise role of cilia and PKD2 during angiogenesis could advance our understanding of pathological angiogenic processes.

EXPERIMENTAL PROCEDURES

Zebrafish Husbandry, Embryo Treatments, and MOs

The zebrafish lines used in this study were *Tg(cmlc2:egfp)* (Huang et al., 2003), *Tg(fli:gal4FF^{ubs}; UAS:kaede)* (Herwig et al., 2011), *Tg(flk1:mCherry)* (Bertrand et al., 2010), *Tg(β-actin:arl13b-egfp)* (Borovina et al., 2010), *Tg(UAS:gcamp3.0; Gal4s1020t)* (Warp et al., 2012), *Tg(fli1a:neGFP)^{y7}* (Roman et al., 2002), and *cup^{tc321}* (Schottenfeld et al., 2007), and were described previously. Morpholinos (MOs) were injected at the one-cell stage and animals were incubated at 28.5°C for 5 hr before treatment with 1-phenyl-2-thiourea (PTU; Sigma Aldrich) to prevent pigment formation. The MOs are further described in Supplemental Experimental Procedures. All zebrafish strains were maintained at the IGBMC under standard husbandry conditions. Animal experiments were approved by the Animal Experimentation Committee of the Institutional Review Board of the IGBMC.

In Vivo Imaging and Correlative Light and Electron Microscopy

Zebrafish embryos were staged, anesthetized with 0.02% tricaine solution (except for Figure 1), mounted in drops of 0.8% low-melting-point agarose (Sigma Aldrich), and imaged with various imaging modalities as described in Supplemental Experimental Procedures.

Heart Imaging and Image Processing

Heart myocardium (*Tg(cmlc2:egfp)*), endocardium, and blood cells (*Tg(fli:gal4FF; UAS:kaede)*) were imaged at 77 frames per second (fps). 4D imaging was performed using consecutive xy(c)tz time-lapse acquisitions. Time series were acquired at a random time in the cardiac cycle and 200–250 frames were acquired. Both channels were acquired simultaneously. Upon completion of a 2D time series at one z section, the optical plane was moved 5 μm and the acquisition was repeated. 4D data sets contained 20–35 z sections and ranged from 100 to 200 μm in total depth. Time series of 2D sections were temporally analyzed using custom-made MATLAB software (Liebling et al., 2005). Realigned 4D data sets were displayed and analyzed using Imaris software (Bitplane AG). Linear deformation of the outflow tract region was performed upon kymograph analysis. The kymograph line was drawn from the center of the cardiac tube perpendicular to the cardiac tube axis (see scheme in Figure S1C). Myocardium and endocardium deformation was quantified by measuring the variation (Δl/l) of length from the outer surface of the cell layer to the center of the cardiac tube.

Blood Cell Imaging and Velocity Measurements

Blood flow was imaged at 77 fps (Figure 1), 29 fps (Figures 3A–3C), 10 fps (Figure 3J), and 250 fps (Figure S4). Blood cells were tracked manually using Fiji or ImageJ. Mean flow velocity values were obtained by averaging instantaneous velocities over a single track. The pulsatility index (PI) was obtained using the following formula ($PI = (Velocity^{Max} - Velocity^{Min})/Velocity^{Mean}$). 3D data sets were analyzed, color-coded, and displayed using Imaris software (Bitplane AG). Maximum projections of ultrafast acquisitions (250 fps; Figure S4G) were used to map flow-carrying vessels and reveal vessel architecture.

Cilia Deflection and Image Processing

Cilia located in the central region of the dorsal aorta were imaged at 29 fps (*Tg(β-actin:Arl13b-GFP)*). Cilia and endothelium (*Tg(β-actin:Arl13b-GFP; flk:mCherry)*) were acquired simultaneously. The GFP signal was used to

Figure 3. Blood Flow Onset Is Mechanically Detected by Primary Cilia and Transduced via a *pkd2*-Dependent Calcium Increase

(A) High-speed confocal imaging at 29 fps and digital tracking in a *Tg (flk1:mCherry; β-actin:Arl13b-egfp)* embryo at 28 hpf. Note the cilium deflection and flow direction (white arrow). See also Movies S13 and S14.

(B) Digital tracking permits the segmentation of cilium outlines. Consecutive outlines were color-coded over time during one deflection phase (210 ms).

(C) Cilia deflection angle and flow velocity (see scheme) were quantified overtime and plotted. Note the correlation between maximum and minimum flow velocity and maximum and minimum flow deflection, respectively (red and green arrows).

(D) Cilia deflection in the DA of 24, 26, and 28 hpf embryos.

(F) Quantification of (D).

(E and G) Calcium content in the developing DA was evaluated and quantified using the endothelial-specific expression of GCAMP3.0 in *Tg(fli:gal4FF; UAS:gcamp3.0)* embryos. GCAMP3.0 intensity was normalized to the average KAEDE intensity observed in distinct embryos.

(H and I) Table and graphical display showing the average cilia deflection observed in 28 hpf control and indicated morphant embryos. See also Movie S15, which presents high-speed confocal imaging at 29 fps and digital tracking in a *Tg(β-actin:Arl13b-egfp)* embryo at 28 hpf injected with the *tnnt2a* MO. Note the absence of cilium deflection over a 210 ms period and random particle movement (blue track). The cilium is not deflected and remains perpendicular to the vessel wall.

(J) Blood flow velocity was quantified using transmission of light in embryos carrying the *Tg(fli:gal4FF; UAS:gcamp3.0)* transgene quantified in (K). Note the absence of flow in *tnnt2a* morphants. See an example in Movie S16.

(K) Calcium content in the developing DA was evaluated in different conditions and quantified using the endothelial-specific expression of GCAMP3.0 in *Tg(fli:gal4FF; UAS:gcamp3.0)* embryos.

(L) Summary graphical representation. The diagram shows that the early developing ECs are sensitive to low flow forces. Protruding and highly sensitive primary cilia behave as flow sensors and allow a fine detection of low but increasing flow forces during blood flow onset. Flow-mediated cilia deflection allows a PKD2-dependent calcium influx in the endothelium.

Error bars depict SEM. Statistical significance was determined by unpaired Student's t test; *$p < 0.05$, **$p < 0.01$, ***$p < 0.001$. See also Figures S3 and S4.

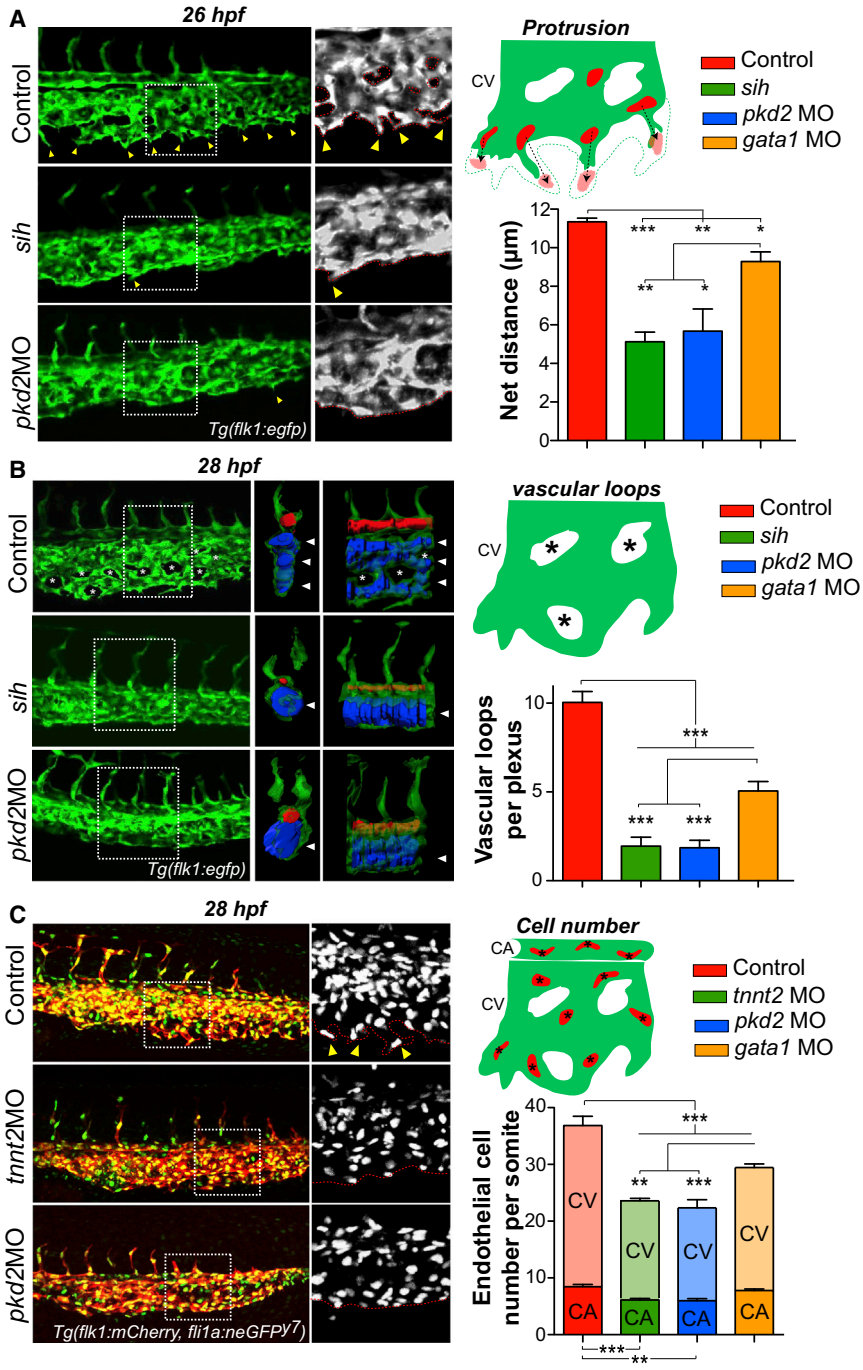

Figure 4. Early Hemodynamics Control Embryonic Angiogenesis

(A) The protrusive activity of the CV was assessed in controls, *sih* mutants, and *pkd2* morphants at 26 hpf. Yellow arrowheads point to vascular sprouts of the CV. Note the absence of such sprouts in both the *sih* mutants and *pkd2* morphants. Using the *Tg(fli1a:neGFP)*^{y7} transgenic line, we tracked the nuclei of ECs at the migration front of the CV (scheme) and followed their movement over a 1 hr period. See also Movie S18. The graph shows the average net distance covered by the tracked cells in control, mutant (*sih*), and morphant (*pkd2* and *gata1*) embryos (between three and four embryos were imaged per condition).

(B) Vascular morphogenesis of the CV was assessed in controls, *sih* mutants, and *pkd2* morphants at 28 hpf. Asterisks point to vascular loops, which are mostly absent in *sih* mutants and *pkd2* morphants (see scheme). 3D models of the vascular lumens of a delimited region (two somites) of the caudal plexus were created and are displayed as orthogonal and side views. The CA is colored in red and the CV is in blue. Images are representative of three to eight embryos imaged per condition. See also Movie S19. Arrowheads point to distinct vessels of the CV. Note that a single vessel is observed in both *sih* mutants and *pkd2* morphants. The graph shows the number of vascular loops present in the CV at 28 hpf.

(C) The overall number of ECs in the caudal plexus (CA+CV) was assessed in controls and *tnnt2a* and *pkd2* morphants at 28 hpf. Yellow arrowheads point to sprouting regions of the CV. Cell number was quantified in the caudal plexus of 28 hpf embryos and normalized per somite (between 6 and 11 embryos were imaged per condition; CA/V, caudal artery/vein).

Error bars depict SEM. Statistical significance was determined by unpaired Student's t test; *$p < 0.05$, **$p < 0.01$, ***$p < 0.001$. See also Figure S4.

retrieve cilia contours using custom MATLAB segmentation software, based on image thresholding and morphological features. The program calculated the most acute angle between the segmented cilia outline and the endothelial surface for each acquired image. Frequency analysis was performed using discrete Fourier transforms of ciliary movement.

Calcium Imaging

For endothelial-specific expression of Gcamp3.0, Tg(fli:gal4FF; UAS:kaede) embryos were crossed with Tg(UAS:GCaMP3; Gal4s1020t), and GCcamp3.0 was imaged as described in Supplemental Experimental Procedures.

Photo-MO Knockdown of *pkd2* and *ift88*

Photo-cleavable MOs were purchased from Genetools. The sense photo-MO (pMO-*pkd2*: 3′-CTT GCGCpGACCTCGAGTA-5′; pMO-*ift88: 3′-ATG GAGAATGTGpATCTTGTCC-5′*) was mixed with a translation-blocking anti-sense MO (MO3-*pkd2*MO: 5′-AGGACGAACGCGACTGGAGCTCA TC-3′; MO1-*ift88: 5′- CTGGGACAAGATGCACAT TCTCCAT-3′*) at a 1.1:1 molar ratio (see Figure S4 for the photo-MO strategy) and injected at the one- to two-cell stage into either *Tg(flk1:egfp)* or *Tg(β-actin:arl13b-egfp)* embryos. Photo-cleavage was performed at 21 hpf (pMO-*ift88*) or 22 hpf (pMO-*pkd2*). A detailed protocol is provided in Supplemental Experimental Procedures.

Immunolabeling

Whole-mount immunocytochemistry was performed as previously described (Obara et al., 2006). More detailed information is provided in Supplemental Experimental Procedures.

Bending Stiffness Estimation

The endothelial cilia biomechanics was modeled as previously described (Young et al., 2012). The cilium was modeled as a beam and the hydrodynamic

load was computed by the local slender-body theory. The bending stiffness was defined as $E_b = M/k$, with k being the curvature and M the moment at a cross-section of the cilium. Several simulations were repeated using flow conditions observed in 26 hpf embryos (Figure 1) by varying the value of E_b until the angle between the cilia tip and the cell base matched the angle measured in vivo (roughly 60°; Figure 3). A range of values for E_b were obtained to cover the variability of the angle between the cilia base and the cell surface (measured and imposed as a boundary condition).

Shear Stress Measurements

Shear stress was calculated as previously described (Vermot et al., 2009).

Statistics

Error bars depict SEM. Statistical significance was determined with GraphPad Prism by unpaired Student's t test (*$p < 0.05$, **$p < 0.01$, ***$p < 0.001$).

Movie Crafting and 3D Modeling

Movie crafting was performed using ImageJ. 3D modeling was performed using Imaris (Bitplane AG).

SUPPLEMENTAL INFORMATION

Supplemental Information includes Supplemental Experimental Procedures, four figures, and 19 movies and can be found with this article online at http://dx.doi.org/10.1016/j.celrep.2014.01.032.

ACKNOWLEDGMENTS

We thank P. Schultz and C. Crucifix for sharing equipment and help with electron tomography. We thank D. Acehan for help with electron tomography. We thank I. Drummond for providing the PKD2 antibody and the pkd2 mutant line (*cup*^{tc321}). We thank M. Affolter, H. Belting, J. Essner, P. Herbomel, and B. Ciruna for providing fish stocks. We thank the staff of the IGBMC imaging center, in particular C. Spiegelhalter, N. Messaddeq, P. Kessler, M. Koch, and D. Hentsch. We thank S. Geschier and S. Gredler of the IGBMC fish facility. We thank D. Wu, W. Supatto, D. Riveline, I. Kulic, and J.B. Freund for critical inputs during the study. This work was supported by HFSP, INSERM, La Ligue Contre le Cancer, FRM, and the Seventh Framework Program (MC-IRG256549 to J.V. and MC-IEF254951 to J.G.G.).

Received: November 15, 2013
Revised: December 20, 2013
Accepted: January 23, 2014
Published: February 20, 2014

REFERENCES

AbouAlaiwi, W.A., Takahashi, M., Mell, B.R., Jones, T.J., Ratnam, S., Kolb, R.J., and Nauli, S.M. (2009). Ciliary polycystin-2 is a mechanosensitive calcium channel involved in nitric oxide signaling cascades. Circ. Res. *104*, 860–869.

Ben Shoham, A., Malkinson, G., Krief, S., Shwartz, Y., Ely, Y., Ferrara, N., Yaniv, K., and Zelzer, E. (2012). S1P1 inhibits sprouting angiogenesis during vascular development. Development *139*, 3859–3869.

Bertrand, J.Y., Chi, N.C., Santoso, B., Teng, S., Stainier, D.Y., and Traver, D. (2010). Haematopoietic stem cells derive directly from aortic endothelium during development. Nature *464*, 108–111.

Borovina, A., Superina, S., Voskas, D., and Ciruna, B. (2010). Vangl2 directs the posterior tilting and asymmetric localization of motile primary cilia. Nat. Cell Biol. *12*, 407–412.

Buschmann, I., Pries, A., Styp-Rekowska, B., Hillmeister, P., Loufrani, L., Henrion, D., Shi, Y., Duelsner, A., Hoefer, I., Gatzke, N., et al. (2010). Pulsatile shear and Gja5 modulate arterial identity and remodeling events during flow-driven arteriogenesis. Development *137*, 2187–2196.

Bussmann, J., Wolfe, S.A., and Siekmann, A.F. (2011). Arterial-venous network formation during brain vascularization involves hemodynamic regulation of chemokine signaling. Development *138*, 1717–1726.

Chen, Q., Jiang, L., Li, C., Hu, D., Bu, J.W., Cai, D., and Du, J.L. (2012). Haemodynamics-driven developmental pruning of brain vasculature in zebrafish. PLoS Biol. *10*, e1001374.

Corti, P., Young, S., Chen, C.Y., Patrick, M.J., Rochon, E.R., Pekkan, K., and Roman, B.L. (2011). Interaction between alk1 and blood flow in the development of arteriovenous malformations. Development *138*, 1573–1582.

Forouhar, A.S., Liebling, M., Hickerson, A., Nasiraei-Moghaddam, A., Tsai, H.J., Hove, J.R., Fraser, S.E., Dickinson, M.E., and Gharib, M. (2006). The embryonic vertebrate heart tube is a dynamic suction pump. Science *312*, 751–753.

Freund, J.B., Goetz, J.G., Hill, K.L., and Vermot, J. (2012). Fluid flows and forces in development: functions, features and biophysical principles. Development *139*, 1229–1245.

Gaengel, K., Niaudet, C., Hagikura, K., Laviña, B., Muhl, L., Hofmann, J.J., Ebarasi, L., Nyström, S., Rymo, S., Chen, L.L., et al. (2012). The sphingosine-1-phosphate receptor S1PR1 restricts sprouting angiogenesis by regulating the interplay between VE-cadherin and VEGFR2. Dev. Cell *23*, 587–599.

Garcia-Gonzalez, M.A., Outeda, P., Zhou, Q., Zhou, F., Menezes, L.F., Qian, F., Huso, D.L., Germino, G.G., Piontek, K.B., and Watnick, T. (2010). Pkd1 and Pkd2 are required for normal placental development. PLoS ONE *5*, 5.

Herbert, S.P., and Stainier, D.Y. (2011). Molecular control of endothelial cell behaviour during blood vessel morphogenesis. Nat. Rev. Mol. Cell Biol. *12*, 551–564.

Herwig, L., Blum, Y., Krudewig, A., Ellertsdottir, E., Lenard, A., Belting, H.G., and Affolter, M. (2011). Distinct cellular mechanisms of blood vessel fusion in the zebrafish embryo. Curr. Biol. *21*, 1942–1948.

Hierck, B.P., Van der Heiden, K., Alkemade, F.E., Van de Pas, S., Van Thienen, J.V., Groenendijk, B.C., Bax, W.H., Van der Laarse, A., Deruiter, M.C., Horrevoets, A.J., and Poelmann, R.E. (2008). Primary cilia sensitize endothelial cells for fluid shear stress. Dev. Dyn. *237*, 725–735.

Hoey, D.A., Downs, M.E., and Jacobs, C.R. (2012). The mechanics of the primary cilium: an intricate structure with complex function. J. Biomech. *45*, 17–26.

Huang, C.J., Tu, C.T., Hsiao, C.D., Hsieh, F.J., and Tsai, H.J. (2003). Germ-line transmission of a myocardium-specific GFP transgene reveals critical regulatory elements in the cardiac myosin light chain 2 promoter of zebrafish. Dev. Dyn. *228*, 30–40.

Iomini, C., Tejada, K., Mo, W., Vaananen, H., and Piperno, G. (2004). Primary cilia of human endothelial cells disassemble under laminar shear stress. J. Cell Biol. *164*, 811–817.

Isogai, S., Horiguchi, M., and Weinstein, B.M. (2001). The vascular anatomy of the developing zebrafish: an atlas of embryonic and early larval development. Dev. Biol. *230*, 278–301.

Isogai, S., Lawson, N.D., Torrealday, S., Horiguchi, M., and Weinstein, B.M. (2003). Angiogenic network formation in the developing vertebrate trunk. Development *130*, 5281–5290.

Jung, B., Obinata, H., Galvani, S., Mendelson, K., Ding, B.S., Skoura, A., Kinzel, B., Brinkmann, V., Rafii, S., Evans, T., and Hla, T. (2012). Flow-regulated endothelial S1P receptor-1 signaling sustains vascular development. Dev. Cell *23*, 600–610.

Kramer-Zucker, A.G., Olale, F., Haycraft, C.J., Yoder, B.K., Schier, A.F., and Drummond, I.A. (2005). Cilia-driven fluid flow in the zebrafish pronephros, brain and Kupffer's vesicle is required for normal organogenesis. Development *132*, 1907–1921.

Laux, D.W., Young, S., Donovan, J.P., Mansfield, C.J., Upton, P.D., and Roman, B.L. (2013). Circulating Bmp10 acts through endothelial Alk1 to mediate flow-dependent arterial quiescence. Development *140*, 3403–3412.

le Noble, F., Moyon, D., Pardanaud, L., Yuan, L., Djonov, V., Matthijsen, R., Bréant, C., Fleury, V., and Eichmann, A. (2004). Flow regulates arterial-venous differentiation in the chick embryo yolk sac. Development *131*, 361–375.

Liebling, M., Forouhar, A.S., Gharib, M., Fraser, S.E., and Dickinson, M.E. (2005). Four-dimensional cardiac imaging in living embryos via postacquisition synchronization of nongated slice sequences. J. Biomed. Opt. *10*, 054001.

McGrath, J., Somlo, S., Makova, S., Tian, X., and Brueckner, M. (2003). Two populations of node monocilia initiate left-right asymmetry in the mouse. Cell *114*, 61–73.

Meder, B., Laufer, C., Hassel, D., Just, S., Marquart, S., Vogel, B., Hess, A., Fishman, M.C., Katus, H.A., and Rottbauer, W. (2009). A single serine in the carboxyl terminus of cardiac essential myosin light chain-1 controls cardiomyocyte contractility in vivo. Circ. Res. *104*, 650–659.

Nauli, S.M., Alenghat, F.J., Luo, Y., Williams, E., Vassilev, P., Li, X., Elia, A.E., Lu, W., Brown, E.M., Quinn, S.J., et al. (2003). Polycystins 1 and 2 mediate mechanosensation in the primary cilium of kidney cells. Nat. Genet. *33*, 129–137.

Nauli, S.M., Kawanabe, Y., Kaminski, J.J., Pearce, W.J., Ingber, D.E., and Zhou, J. (2008). Endothelial cilia are fluid shear sensors that regulate calcium signaling and nitric oxide production through polycystin-1. Circulation *117*, 1161–1171.

Nicoli, S., Standley, C., Walker, P., Hurlstone, A., Fogarty, K.E., and Lawson, N.D. (2010). MicroRNA-mediated integration of haemodynamics and Vegf signalling during angiogenesis. Nature *464*, 1196–1200.

Obara, T., Mangos, S., Liu, Y., Zhao, J., Wiessner, S., Kramer-Zucker, A.G., Olale, F., Schier, A.F., and Drummond, I.A. (2006). Polycystin-2 immunolocalization and function in zebrafish. J. Am. Soc. Nephrol. *17*, 2706–2718.

Oh, E.C., and Katsanis, N. (2012). Cilia in vertebrate development and disease. Development *139*, 443–448.

Potente, M., Gerhardt, H., and Carmeliet, P. (2011). Basic and therapeutic aspects of angiogenesis. Cell *146*, 873–887.

Roman, B.L., Pham, V.N., Lawson, N.D., Kulik, M., Childs, S., Lekven, A.C., Garrity, D.M., Moon, R.T., Fishman, M.C., Lechleider, R.J., and Weinstein, B.M. (2002). Disruption of acvrl1 increases endothelial cell number in zebrafish cranial vessels. Development *129*, 3009–3019.

Rydholm, S., Zwartz, G., Kowalewski, J.M., Kamali-Zare, P., Frisk, T., and Brismar, H. (2010). Mechanical properties of primary cilia regulate the response to fluid flow. Am. J. Physiol. Renal Physiol. *298*, F1096–F1102.

Schottenfeld, J., Sullivan-Brown, J., and Burdine, R.D. (2007). Zebrafish curly up encodes a Pkd2 ortholog that restricts left-side-specific expression of southpaw. Development *134*, 1605–1615.

Sehnert, A.J., Huq, A., Weinstein, B.M., Walker, C., Fishman, M., and Stainier, D.Y. (2002). Cardiac troponin T is essential in sarcomere assembly and cardiac contractility. Nat. Genet. *31*, 106–110.

Supatto, W., and Vermot, J. (2011). From cilia hydrodynamics to zebrafish embryonic development. Curr. Top. Dev. Biol. *95*, 33–66.

Tsujikawa, M., and Malicki, J. (2004). Intraflagellar transport genes are essential for differentiation and survival of vertebrate sensory neurons. Neuron *42*, 703–716.

Vermot, J., Forouhar, A.S., Liebling, M., Wu, D., Plummer, D., Gharib, M., and Fraser, S.E. (2009). Reversing blood flows act through klf2a to ensure normal valvulogenesis in the developing heart. PLoS Biol. *7*, e1000246.

Warp, E., Agarwal, G., Wyart, C., Friedmann, D., Oldfield, C.S., Conner, A., Del Bene, F., Arrenberg, A.B., Baier, H., and Isacoff, E.Y. (2012). Emergence of patterned activity in the developing zebrafish spinal cord. Current biology: CB *22*, 93–102.

Yoshiba, S., Shiratori, H., Kuo, I.Y., Kawasumi, A., Shinohara, K., Nonaka, S., Asai, Y., Sasaki, G., Belo, J.A., Sasaki, H., et al. (2012). Cilia at the node of mouse embryos sense fluid flow for left-right determination via Pkd2. Science *338*, 226–231.

Young, Y.N., Downs, M., and Jacobs, C.R. (2012). Dynamics of the primary cilium in shear flow. Biophys. J. *103*, 629–639.